PHYSICAL REVIEW C **97**, 054602 (2018)

Dynamics of Db isotopes formed in reactions induced by ^{238}U, ^{248}Cm, and ^{249}Bk across the Coulomb barrier

Gurjit Kaur,[1] Kirandeep Sandhu,[2] Amandeep Kaur,[1] and Manoj K. Sharma[1,*]
[1]*School of Physics and Materials Science, Thapar Institute of Engineering and Technology, Patiala-147004, India*
[2]*Department of Physics, GSSDGS Khalsa College, Patiala-147001, India*

(Received 27 February 2018; published 3 May 2018)

The dynamical cluster decay model is employed to investigate the decay of ^{265}Db* and ^{267}Db* nuclei, formed in the ^{27}Al + ^{238}U, ^{18}O + ^{249}Bk, and ^{19}F + ^{248}Cm hot fusion reactions at energies around the Coulomb barrier. First, the fission dynamics of the ^{27}Al + ^{238}U reaction is explored by investigating the fragmentation and preformation yield of the reaction. The symmetric mass distribution of the fission fragments is observed for ^{265}Db* nucleus, when static β_{2i} deformations are used within hot optimum orientation approach. However, the mass split gets broaden for the use of β_{2i}-dynamical hot configuration of the fragments and becomes clearly asymmetric for the cold-static-deformed approach. Within the application of cold orientations of fragments, a new fission channel is observed at mass asymmetry $\eta = 0.29$. In addition to ^{238}U-induced reaction, the work is carried out to address the fission and neutron evaporation cross sections of ^{267}Db* nucleus formed via ^{19}F + ^{248}Cm and ^{18}O + ^{249}Bk reactions, besides a comprehensive analysis of fusion and capture processes. Higher fusion cross sections and compound nucleus formation probabilities (P_{CN}) are obtained for the ^{18}O + ^{249}Bk reaction, as larger mass asymmetry in the entrance channel leads to reduced Coulomb factor. Finally, the role of sticking (I_S) and nonsticking (I_{NS}) moments of inertia is analyzed for the $4n$ and $5n$ channels of ^{267}Db* nuclear system.

DOI: 10.1103/PhysRevC.97.054602

I. INTRODUCTION

The investigation of the reaction dynamics involving the evolution of odd-Z superheavy nuclei is essential to examine the unexplored region of the nuclear chart. The existence of unpaired nucleons in the odd-Z nuclei effect the structure and reaction dynamics to a reasonable extent, which could be investigated through the dynamical study of the superheavy nuclei [1]. Therefore, an attempt is made to investigate the decay paths of dubnium ($Z = 105$) nucleus formed in different hot fusion reactions. This nucleus has been of great interest for past few decades and its first signature was reported by the Joint Institute for Nuclear Research in the analysis of the ^{22}Ne + ^{243}Am reaction [2]. Subsequently, various isotopes of Db were synthesized in hot and cold fusion reactions. The excitation functions for the $1n$ and $2n$ exit channels of the ^{208}Pb(^{51}V, xn)$^{259-x}$Db and ^{209}Bi(^{50}Ti, xn)$^{259-x}$Db reactions were measured at Lawrence Berkeley National Laboratory [3]. In addition to this, the capture and fusion processes were also obtained for ^{259}Db* and ^{265}Db* nuclear systems, respectively formed in the ^{50}Ti + ^{209}Bi [4] and ^{27}Al + ^{238}U [5] reactions. To have a comprehensive knowledge about the decay of Db nuclei, recently the ^{248}Cm(^{19}F, xn)$^{267-x}$Db and ^{249}Bk(^{18}O, xn)$^{267-x}$Db reactions were compared by Haba *et al.* [6] for the production of Db isotopes through $4n$ and $5n$ emissions, and the same are tested here in the framework of the dynamical cluster decay model (DCM) [7–12]. The individual excitation functions for ^{263}Db and ^{262}Db nuclei are evaluated across the Coulomb barrier energies. The channel cross sections are calculated for both sticking and nonsticking moments of inertia (I_S and I_{NS}, respectively), by including the quadrupole (β_{2i}) deformations and "hot-optimum" orientations. The $4n$ channel could be addressed via I_S and I_{NS} approaches, whereas nonsticking (I_{NS}) approach seems favorable to address the $5n$ cross sections, particularly for the ^{18}O + ^{249}Bk reaction.

In addition to the addressal of the evaporation residue cross sections, the separation between the capture and fusion events is the main quest to handle the superheavy reaction dynamics. The origin of the noncompound nuclear processes, such as quasifission, quasielastic, and deep-inelastic events, always hinder the superheavy compound nucleus formation [13], hence the fusion cross sections generally have lower magnitude as compare to the capture cross sections. The reason lies in the fact that the fusion of two heavy nuclei is governed through various factors such as excitation energy, Coulomb interactions, entrance channel mass asymmetry, deformation parameters, and barrier characteristics of the reaction partners, etc. Keeping this in mind, the fusion mechanism of the ^{19}F + ^{248}Cm $\rightarrow$ ^{267}Db* and ^{18}O + ^{249}Bk $\rightarrow$ ^{267}Db* reactions is analyzed through the Wong model [14], using the barrier characteristics such as barrier height (V_B), barrier position (R_B), curvature ($\hbar\omega$), etc. In addition to the above reactions, the uranium-induced hot fusion reaction leading to ^{265}Db* nucleus is also investigated within the framework of the DCM model [7–12]. Within this methodology, the symmetric mass distribution of the fission fragments is governed through the hot-optimum orientations of the fragments, suggesting that fusion-fission is a main decay mode for ^{265}Db* and ^{267}Db* nuclei. However, the contribution of the symmetric fission

---

[*] msharma@thapar.edu

fragments gets significantly suppressed for the use of cold-elongated configurations of the fragments, subsequently giving rise to new fission valley with mass asymmetry $\eta = 0.29$. It is relevant to mention that the compact configuration of the composite system is achieved usually at the energies higher than Coulomb barrier, where the probability of the head-on interaction is prominent. On the other hand, elongated configuration of the nuclear system is perceived at the sub-barrier region exhibiting higher interaction radius and lower barrier height [15]. However, in the present work, the interaction and decay analysis is observed near the Coulomb barrier, where both configurations may compete, and their barrier properties may help to distinguish between different events for the $^{19}\mathrm{F} + {}^{248}\mathrm{Cm}$, $^{18}\mathrm{O} + {}^{249}\mathrm{Bk}$, and $^{27}\mathrm{Al} + {}^{238}\mathrm{U}$ reactions.

In view of the above discussion, the paper is organized as follows: Section II gives a brief overview of the methodology, which includes the introduction of the Wong and the DCM models. Various parameters of the models are briefly discussed in this section. Subsequent to this, the details of calculations and results are discussed in Sec. III. Finally, the summary and conclusions are presented in Sec. IV.

II. METHODOLOGY

This section comprises two subsections, Sec. II A and Sec. II B. Capture and fusion cross sections, in addition to compound nucleus formation probability (P_{CN}), studied in the present work are discussed in Sec. II A. A brief description of the DCM model is given in Sec. II B.

A. Capture and fusion cross sections

The capture cross section (σ_{Cap}), in terms of angular-momentum (ℓ) partial waves, for two deformed and oriented nuclei (with orientation angles θ_i), lying in the same planes and colliding with center-of-mass energy $\mathrm{E}_{\mathrm{c.m.}}$, is

$$\sigma_{\mathrm{Cap}}(E_{\mathrm{c.m.}},\theta_i) = \sum_{\ell=0}^{\infty}\sigma_\ell = \frac{\pi}{k^2}\sum_{\ell=0}^{\infty}(2\ell+1)P_\ell \tag{1}$$

with $\mathrm{k} = \sqrt{\frac{2\mu E_{\mathrm{c.m.}}}{\hbar^2}}$ and μ is the reduced mass, P_ℓ is the transmission coefficient for each ℓ which describes the penetrability of total interaction barrier $V_T^\ell(\mathrm{R})$. This potential barrier for deformed and oriented nuclei is the sum of Coulomb, proximity, and angular-momentum potentials $[V_T^\ell(R) = V_C + V_P + V_\ell]$ [10,11].

The penetrability P_ℓ, used in Eq. (1), is defined as

$$P_\ell = \left\{1 + \exp\left[\frac{2\pi\left(V_B^\ell - E_{\mathrm{c.m.}}\right)}{\hbar\omega_\ell}\right]\right\}^{-1}. \tag{2}$$

In Eq. (2), Hill Wheeler approximation [16] is applied to calculate the penetrability. In such an approximation, the dependance of transmission probability is worked out in terms of fusion barrier height V_B^ℓ and curvature $\hbar\omega_\ell$ $(E_{\mathrm{c.m.}},\theta_i)$. There are alternative methods, such as the Wentzel-Kramers-Brillouin (WKB) method [17], where the integration over the whole barrier is taken. In the recent past, one of us and collaborators made a comparison of both the approximations, i.e., Hill Wheeler and WKB in Ref. [18], and found that either of the two methods may be applied for the addressal of the fusion barrier. In penetrability expression, $\hbar\omega_\ell$ is evaluated at the barrier position $R = R_B^\ell$ corresponding to barrier height V_B^ℓ and is given as

$$\hbar\omega_\ell(E_{\mathrm{c.m.}},\theta_i) = \hbar\left[\left|d^2V_T^\ell(R)/dR^2\right|_{R=R_B^\ell}/\mu\right]^{1/2} \tag{3}$$

with R_B^ℓ obtained from the condition $|dV_T^\ell(R)/dR|_{R=R_B^\ell} = 0$. Instead of solving Eq. (1) explicitly, which requires the complete ℓ-dependent potentials V_T^ℓ $(R,\, E_{\mathrm{c.m.}},\, \theta_i)$, Wong [14] carried out the ℓ summation approximately under specific conditions: (i) $\hbar\omega_\ell \approx \hbar\omega_0$ and (ii) $V_B^\ell \approx V_B^0 + \frac{\hbar^2\ell(\ell+1)}{2\mu R_B^0 2}$, which means to assume $R_B^\ell \approx R_B^0$ also. Using these approximations and replacing the ℓ summation in Eq. (1) by an integral gives the $\ell = 0$ barrier-based Wong formula

$$\sigma_{\mathrm{Cap}}(E_{\mathrm{c.m.}},\theta_i) = \frac{R_B^{02}\hbar\omega_0}{2E_{\mathrm{c.m.}}}\ln\left\{1+\exp\left[\frac{2\pi}{\hbar\omega_0}\left(E_{\mathrm{c.m.}} - V_B^0\right)\right]\right\}. \tag{4}$$

In above expression, $\sigma_{\mathrm{Cap}}(E_{\mathrm{c.m.}},\theta_i)$ is calculated for each orientation and then integrated over angle θ_i $(i = 1,2)$ to a given final capture cross section as

$$\sigma_{\mathrm{Cap}}(E_{\mathrm{c.m.}}) = \int_{\theta_i=0}^{\pi/2}\sigma(E_{\mathrm{c.m.}},\theta_i)\sin\theta_1 d\theta_1 \sin\theta_2 d\theta_2. \tag{5}$$

The fusion cross section for superheavy nuclei constitutes only a part of the capture cross section, so the fusion cross section is always equal to or less than the capture cross section and is expressed as

$$\sigma_{\mathrm{fusion}}(E_{\mathrm{c.m.}},\theta_i) = \frac{\pi}{k^2}\sum_{\ell=0}^{\infty}(2\ell+1)P_\ell P_{\mathrm{CN}}. \tag{6}$$

In above equation, P_{CN} is the compound nucleus formation probability. The mean fissility parameter- (x_m) dependent formation probability (P_{CN}) is defined as the linear combination of the effective fissility parameter x_{eff} and compound nucleus fissility parameter x_{CN}. The mean fissility parameter is defined as [19]

$$x_m = 0.75x_{\mathrm{eff}} + 0.25x_{\mathrm{CN}}. \tag{7}$$

The compound nucleus fissility parameter x_{CN} is the ratio of competing Coulomb and nuclear forces for compact shapes and is given by [20]

$$x_{\mathrm{CN}} = \frac{(Z^2/A)}{(Z^2/A)_{\mathrm{crit}}} = \frac{(Z^2/A)}{50.883[1 - 1.7826I^2]}, \tag{8}$$

where $I = (A - 2Z)/A$ is the relative neutron excess of compound nucleus. The effective fissility parameter x_{eff} which includes the effect of mass and charge asymmetry is as follows [20]:

$$x_{\mathrm{eff}} = \frac{4Z_1Z_2/\left[A_1^{1/3}A_2^{1/3}\left(A_1^{1/3} + A_2^{1/3}\right)\right]}{50.883[1 - 1.7826I^2]}. \tag{9}$$

The value of P_{CN}^0, which is the “asymptotic” fusion probability, was proposed by Zagrebaev and Greiner [21]. It depends on the above parameters of the colliding nuclei by the relation

$$P^0_{\mathrm{CN}} = \frac{1}{1+\exp(x_m - \xi)/\tau}. \tag{10}$$

The parameters of Eq. (10), giving better agreement with the estimated values of P^0_{CN} for reactions with actinides targets, are defined as $\tau = 0.0226$ and $\xi = 0.721$ [19]. The energy dependence of fusion probability can be approximated by simple relation as [21]

$$P_{\mathrm{CN}}(E^*,\ell) = \frac{P^0_{\mathrm{CN}}}{1+\exp[(E^*_B - E^*_{\mathrm{CN}})/\triangle]}. \tag{11}$$

Here E^*_B is the excitation energy of compound nucleus equal to bass barrier, E^*_{CN} is the excitation energy, and $\triangle$ is the adjustable parameter of about 4 MeV.

B. The DCM

The DCM [7–12] is based on quantum mechanical fragmentation theory (QMFT) [22,23], which uses two-center shell model (TCSM) by the authors of Ref. [24]. It provides a suitable platform for the study of microscopic effects when two spherical asymmetric nuclei combine from two different states to one or vice versa. This model is further modified by Gherghescu [25] in which instead of spherical, two ellipsoidal deformed nuclei are taken into account for more realistic calculations of two interacting nuclei. QMFT in binary fragmentation is based on collective coordinates of mass (and charge) asymmetries $\eta_A = (A_1 - A_2)/(A_1 + A_2)$ (1 and 2 stand, respectively, for heavy and light fragments), the relative separation R, multipole deformations $\beta_{\lambda i}$ (λ = 2, 3, 4), and orientations θ_i (i = 1,2) of two nuclei or fragments. In terms of these coordinates the decay or fragment's production cross section for ℓ-partial waves is given by

$$\sigma = \sum_{\ell=0}^{\ell_{\max}} \sigma_\ell = \frac{\pi}{k^2}\sum_{\ell=0}^{\ell_{\max}}(2\ell+1)P_0 P; \quad k = \sqrt{\frac{2\mu E_{\mathrm{c.m.}}}{\hbar^2}}, \tag{12}$$

where $\mu = [A_1A_2/(A_1+A_2)]m$ is the reduced mass and $\ell_{\max}$ is the maximum angular momentum, decided at a point where neutron evaporation cross section becomes negligibly small, $\sigma_{\mathrm{ER}} \rightarrow 0$. Using this equation, DCM calculates the cross sections for different constituents (σ_{ER}, σ_{ff} etc.) as

$$\sigma_{\mathrm{ER}} = \sum_{A_2=1}^{4or5} \sigma(A_1,A_2) \quad \text{and} \quad \sigma_{ff} = 2\sum_{A_2=(A/2)-20}^{A/2} \sigma(A_1,A_2). \tag{13}$$

In Eq. (12), P_0 is the probability with which the cluster or fragment is preformed before it comes out of composite system by penetrating the potential barrier. It is a relative quantity i.e., a slight change in the potential for any one of the fragment leads to redistribution of P_0 among all the fragments. This probability is defined as

$$P_0 = \sum_{\nu=0}^{\infty} |\psi^\nu(\eta(A_i))|^2 \sqrt{B_{\eta\eta}}\,\frac{2}{A_{\mathrm{CN}}}\exp(-E^\nu/T). \tag{14}$$

It refers to η motion and is obtained by solving the stationary Schrödinger equation in mass fragmentation coordinates (η) at fixed $R = R_a$. The mass parameters $B_{\eta\eta}$, used in Eq. (14), are the smooth hydrodynamical masses [26]. Alternatively, one may use the shell corrected cranking masses which are based on shell model [27]. The cranking masses are about one order of magnitude smaller than the classical hydrodynamical masses [28], and hence the magnitude of preformation probability reduces accordingly. Malik *et al.* [29] suggested that the hydrodynamical masses on average give reasonable agreement with microscopic cranking calculations with slight modification in magnitude. Therefore, the hydrodynamical masses are used in the present work for the sake of simplicity. The fragmentation potential $V_R(\eta,T)$ used to solve Schrödinger equation is defined as

$$\begin{aligned} V_R(\eta,T) = {} & \sum_{i=1}^{2} V_{\mathrm{LDM}}(A_i,Z_i,T) + \sum_{i=1}^{2}\delta U_i \exp\left(-T^2/T_0^2\right) \\ & + V_C(R,Z_i,\beta_{\lambda i},\theta_i,T) + V_P(R,A_i,\beta_{\lambda i},\theta_i,T) \\ & + V_\ell(R,A_i,\beta_{\lambda i},\theta_i,T). \end{aligned} \tag{15}$$

Here V_C, V_P, and V_ℓ are, respectively, the T dependent, Coulomb, nuclear proximity, and centrifugal potentials for deformed, oriented nuclei. The binding energies in the above equation are calculated as the Strutinsky macromicroscopic method and divided into two components, i.e., V_{LDM} and δU. V_{LDM} is the T-dependent liquid drop energy of Davidson *et al.* [30], based on the semiempirical mass formula of Seeger [31]. The microscopic shell corrections δU are the "empirical" estimates of Myers and Swiatecki [32], which are taken as T dependent. It is relevant to mention that alternative approaches like *two-center shell model*, *Strutinsky method*, etc., are also available in the literature for the calculations of shell effects. In TCSM [24], shell corrections are derived from the single-particle potential with two-center level scheme and in its updated version, i.e., deformed two-center shell model [25]; the shape parameters are also included in calculations of microscopic effects. Strutinsky method–based shell-model calculations are derived from inhomogeneous distribution of nucleons as a function of deformations and their energy effects [33]. It will be of interest to explore the role of the above-mentioned shell corrections in the framework of DCM in the near future. The sum of macromicroscopic components is used to calculate the experimental binding energies of Audi *et al.* [34] or the one of Möller *et al.* [35] wherever the same are not available. The centrifugal potential of the nucleus mentioned above in Eq. (15) is given by

$$V_\ell(R,A_i,\beta_{\lambda i},\theta_i,T) = \frac{\hbar^2\ell(\ell+1)}{2I}. \tag{16}$$

Note that I is the moment of inertia and can be calculated by various methods, but in the present work we use two approaches as (i) the sticking limit in which individual masses/charges are included in addition to reduced masses and is given by $I = I_S = \mu R^2 + \frac{2}{5}A_1 m R_1^2(\alpha_1,T) + \frac{2}{5}A_2 m R_2^2(\alpha_2,T)$ and (ii) within nonsticking limit, the moment of inertia is given by $I = I_{\mathrm{NS}} = \mu R^2$. It is relevant to mention here that the values of angular momentum extracted experimentally are generally based on moment of inertia in the nonsticking limit. The Coulomb potential for a multipole-multipole interactions and two nonoverlapping charge distributions [14,36] is given by

$$V_C(R,Z_i,\beta_{\lambda i},\theta_i,T) = \frac{Z_1 Z_2 e^2}{R} + 3Z_1 Z_2 e^2 \times \sum_{\lambda,i=1,2} \frac{R_i^{\lambda}(\alpha_i)}{(2\lambda+1)R^{\lambda+1}} \times Y_{\lambda}^{(0)}(\theta_i)\left[\beta_{\lambda i} + \frac{4}{7}\beta_{\lambda i}^2 Y_{\lambda}^{(0)}(\theta_i)\right]. \tag{17}$$

Here $Y_{\lambda}^{(0)}(\theta_i)$ are the spherical harmonic functions; the orientation angle θ_i is the angle between the nuclear symmetry axis and the collision Z axis, measured in the counter clockwise direction from the axis of collision; and angle α_i is the angle between the symmetry axis and the radius vector of the colliding nucleus, measured in the clockwise direction from the symmetry axis. The orientations are the "optimum" orientations of the "hot" and "cold" processes [37] and the deformation parameters ($\beta_{\lambda i}$) of the nuclei are taken from the tables of Möller *et al.* [35]. Further, the temperature-dependent deformations [38] are also introduced via relation $\beta_{\lambda i}(T) = \exp(-T/T_0)\beta_{\lambda i}(0)$. Here $\beta_{\lambda i}(0)$ are the static deformations and T_0 is the temperature of the nucleus at which shell effects start to vanish (here $T_0 = 1.5$ MeV).

The T-dependent nuclear proximity potential [39] for deformed, orientated nuclei is given by

$$V_P[s_0(T)] = 4\pi \bar{R}\gamma b(T)\Phi[s_0(T)], \tag{18}$$

where $b(T) = 0.99(1 + 0.009T^2)$ is the nuclear surface thickness, γ is the surface energy constant, and $\bar{R}(T)$ is the mean curvature radius. Φ is a universal function which is independent of the shapes of nuclei or the geometry of the nuclear system but depends on minimum separation distance $s_0(T)$.

The penetration probability P in Eq. (12) refers to R motion and is the quantum mechanical tunneling probability of outgoing fragments. It is calculated by using the WKB integral. For more details, we refer the reader to Refs. [7–12]. The first turning point (R_a) in the penetration path is defined as

$$\begin{aligned} R_a &= R_1(\alpha_1,T) + R_2(\alpha_2,T) + \Delta R \\ &= R_t(\alpha,T) + \Delta R \end{aligned} \tag{19}$$

with radius vectors

$$R_i(\alpha_i,T) = R_{0i}(T)\left[1 + \sum_{\lambda} \beta_{\lambda i} Y_{\lambda}^{(0)}(\alpha_i)\right]. \tag{20}$$

The R_{0i}(T) is T-dependent nuclear radii of the equivalent spherical nuclei, taken from [40] as

$$R_{0i}(T) = \left[1.28A_i^{1/3} - 0.76 + 0.8A_i^{-1/3}\right](1 + 0.0007T^2). \tag{21}$$

III. CALCULATIONS AND DISCUSSIONS

The work carried out in the present analysis is based on the prescription given in Sec. II and is divided into two subparts. In Sec. III A, the dynamics of the ^{27}Al + ^{238}U reaction leading to ^{265}Db* superheavy nucleus is examined, and fusion-fission (ff) cross sections are calculated at near barrier energies. In view of earlier work on DCM [8], the magic numbers in superheavy region are taken as $Z = 120$ and $N = 184$ to address the fission cross sections. The fragmentation potentials and preformation probabilities are analyzed to address the fragmentation of the ^{238}U-induced reaction. Following this, Sec. III B presents the evolution of ^{267}Db* nuclear system formed in the ^{19}F + ^{248}Cm ($\eta = 0.857$) and ^{18}O + ^{249}Bk ($\eta = 0.865$) reactions, and an attempt is made to predict the capture and fusion-fission cross sections. In addition to this, the neutron evaporation residue cross sections are also investigated for the same nucleus, to have a comprehensive idea of the dynamics involved.

A. The fission dynamics of the ^{265}Db* nucleus

In order to explore the dynamics of the ^{27}Al + ^{238}U → ^{265}Db* reaction, the fragmentation potential for the ^{265}Db* nucleus is plotted in Fig. 1(b) by including β_{2i}-static deformations and hot optimum orientations. Figure 1(b) is

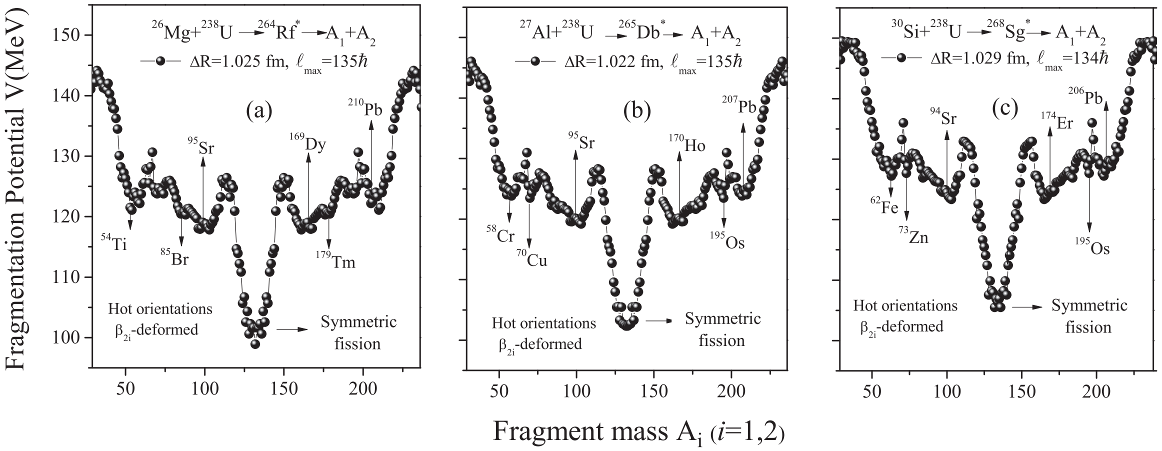

FIG. 1. (a) Fragmentation potential $V(\eta,R)$ plotted as a function of fragment mass for the decay of (a) ^{264}Rf*, (b) ^{265}Db*, and (c) ^{268}Sg* nuclei formed in the ^{238}U-induced reaction at fixed neck-length parameter (ΔR) and angular momentum ($\ell_{\max}$) values, for static-β_{2i}-deformed cases.

plotted for the wide mass range, in which symmetric mass division of the fission fragments is observed. Though some local minima's at ^{58}Cr, ^{70}Cu, and ^{95}Sr nuclei are observed, along with their complementary ($A_1 = A - A_2$) fragments, but the dominance of the symmetric fragmentation depicts that symmetric fission is the main contributor in the dynamics of ^{265}Db* nucleus, when hot-compact deformed fragmentation is employed. Figures 1(a) and 1(c) are also plotted here to observe the fragmentation behavior of the neighboring ^{264}Rf* and ^{268}Sg* nuclei, so that a comparative analysis be carried out to address the decay of light superheavy mass nuclei. It is important to mention that these fragmentation potentials are plotted at energies around the barrier. The decay of ^{268}Sg* nucleus at center-of-mass energy $E_{\mathrm{c.m.}} = 144$ MeV was studied in the previous work [10], but Fig. 1(c) is plotted here to compare its fragmentation behavior with ^{264}Rf* and ^{265}Db* nuclei, as mentioned above. Similar results are observed from Figs. 1(a) and 1(c), favoring symmetric mass fragmentation as the dominant decay channels. Hence one may conclude that for the light superheavy mass range, symmetric distribution of fragmentation is preferred for the hot compact orientations, which becomes highly asymmetric for the heavier superheavy nuclei such as $Z = 115$ and 117 [9]. The magnitude of the neck-length parameter (ΔR) and maximum value of the angular momentum (ℓ_{max}) remains almost constant for the decay of these nuclei. It is important to mention that the decay fragments may vary while going from $Z = 104$ to $Z = 106$, such as ^{54}Ti, ^{58}Cr, and ^{62}Fe fragments appear at first valley, respectively, for ^{264}Rf*, ^{265}Db*, and ^{268}Sg* nuclei. In concurrence to this, different isotopes of lead (Pb) as their complementary fragments are also mentioned in Fig. 1, which may be related to the possible occurrence of the quasifission process.

In the present analysis, mainly two set of orientation approaches are employed in Figs. 2(a) and 2(b) and then Fig. 2(c), respectively, for hot and cold configurations. The hot orientations of the fragments lead to compact structures with the lowest radius and a higher barrier. On the other hand, elongated configurations with a lower barrier and higher radius are perceived for the cold-oriented nuclei. In Fig. 2(a), we started with the preformation probability (P_0), plotted for the static-deformed and hot orientations of the fragments. The result of this figure may be correlated with the one plotted in Fig. 1(b) for fragmentation potential. In this figure, the decay of ^{265}Db* compound nucleus clearly shows the symmetric mass division of the fission fragments, as analyzed in Fig. 1(b). The appearance of Pb peaks in the decay path is generally associated with the phenomenon of the quasifission, but here the contribution of Pb valley is quite small as the preformation probability for this region is negligible as compared to the symmetric fragments. Similarly, the preformation probability for ^{95}Sr and its complementary fragment ^{170}Ho is larger than the Pb valley but still negligibly small as compared to the preformation factor for the fission region of the ^{265}Db* nucleus. Hence the decay of the ^{265}Db* nucleus is mainly characterized by the fusion-fission process while including static hot-compact orientations of the decay fragments.

In Fig. 2(b) the decay structure is significantly modified after the inclusion of dynamical (T dependent) β_2 deformations within hot orientation approach for the ^{265}Db* nucleus (see Sec. II). More fragments start contributing and relatively broader peak is observed for the fission fragments with $\frac{A}{2} \pm 25$, which otherwise remains $\frac{A}{2} \pm 15$ for the previous case (static β_2 deformations). Broadly speaking, the symmetric yield starts broadening when the static β_2 deformations are replaced by dynamic β_2 deformations in the fragmentation analysis. Interestingly, the peaks around ^{95}Sr and ^{170}Ho, having negligible contribution as depicted in Fig. 2(a), start contributing significantly towards fission cross sections when a dynamical hot-fragmentation approach is applied. It is important to illustrate that majority of the minimized fragments near ^{95}Sr and ^{170}Ho peaks, ranging $A_2 = 85-110$ (and the complementary nuclei)

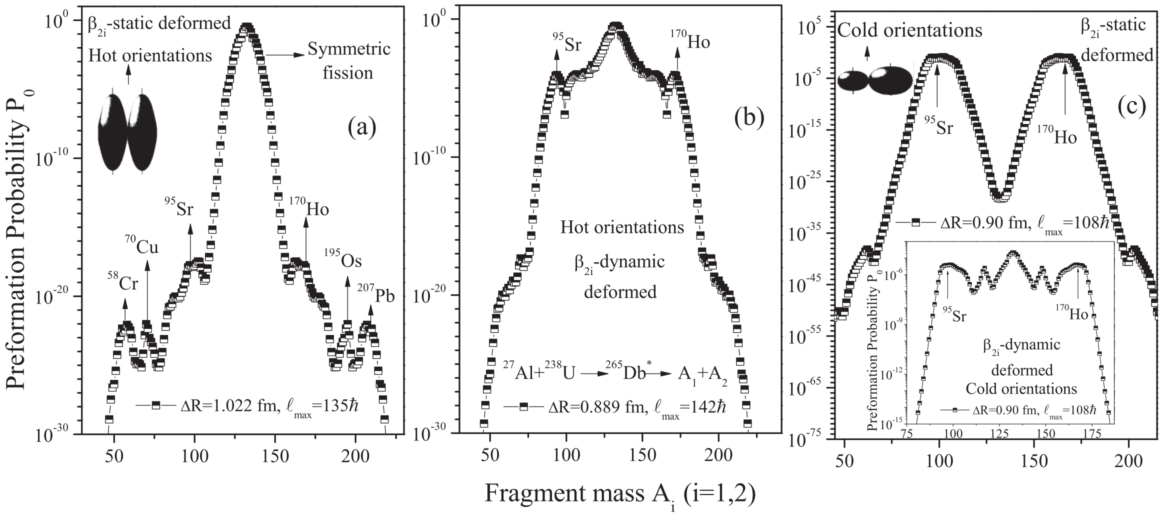

FIG. 2. Preformation probability (P_0), plotted as a function of fragment mass for the decay of ^{265}Db* nucleus using (a) hot static-deformed, (b) hot dynamic-deformed, and (c) cold static-deformed approaches. The figures are useful to extract the knowledge about different decay mechanisms and further used to calculate the fusion-fission cross sections. The inset of panel (c) is same as that of the remaining figures but plotted for the cold dynamic deformations of the nuclei.

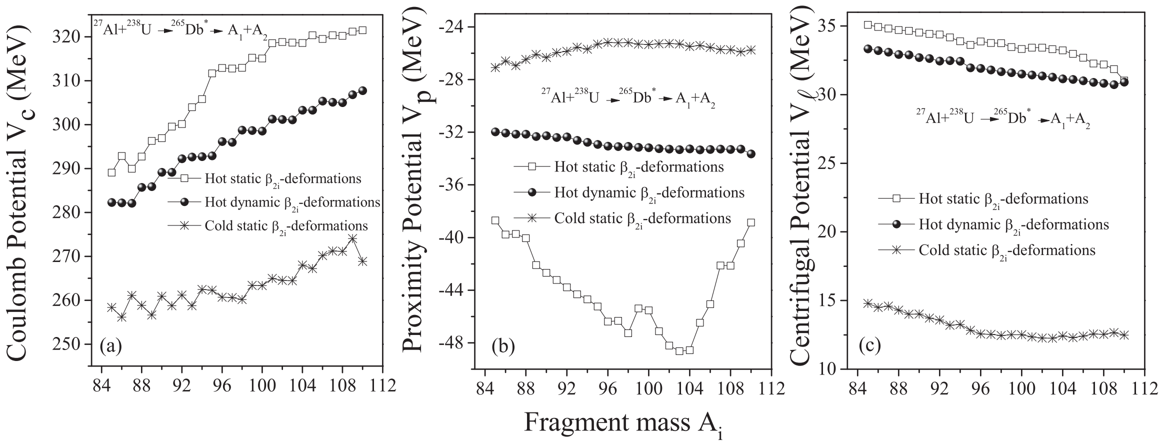

FIG. 3. Variation of the (a) Coulomb (V_C), (b) proximity (V_P, Prox-1977), and (c) centrifugal (V_ℓ) potentials for the fragments lying in range $A_2 = 85-110$ by including the static and dynamic hot-deformed configurations, along with static cold orientations of the decay fragments.

are prolate deformed. The interaction of prolate-prolate nuclei leads to the compact shape at minimum possible magnitude of the R (fm). At this R (fm), the Coulomb, proximity, and centrifugal potentials are calculated as shown in Figs. 3(a), 3(b) and 3(c), respectively for $A_2 = 85-110$ fragments. It may be noticed that, the centrifugal and Coulomb potentials vary inversely with R (fm), given by Eqs. (16) and (17), respectively. However, the proximity part of the total potential has direct dependance on the radius, i.e., $V_P \propto R$. The comparison of Figs. 2(a) and 2(b) can be carried out by arguing the fact that the R (fm), which is fixed for the static-deformed case, starts increasing for the dynamic case as the deformations start diminishing with temperature. With increase in the radius parameters, given by Eq. (20) in Sec. II, the V_C and V_ℓ starts decreasing, as shown in Figs. 3(a) and 3(c), respectively. However, Fig. 3(b) shows that V_P increases in the magnitude as compared to the static-deformed case. The decrease in the magnitude of V_C and V_ℓ is relatively larger and compensates for the increased magnitude of the proximity potential. Hence the overall fragmentation $(V_C + V_P + V_\ell + BE)$ of $A_2 = 85-110$ nuclei decreases, and the preformation factor shows increment for the hot dynamic deformation of the nuclei, which otherwise shows a low preformation factor for the static-deformed case.

A purely asymmetric distribution of fragments is observed in Fig. 2(c) when the calculations are done using static cold orientations. The preformation yield of the symmetric fragments $\frac{A}{2} \pm 15$ reduces significantly for cold-orientated nuclei, which otherwise shows dominance in Fig. 2(a), plotted for the static hot orientations of the decaying fragments. The contribution of the asymmetric cold oriented fragments corresponds the fission peaks with mass asymmetry $\eta = (A_H - A_L)/(A_H + A_L) = 0.29$. Such a fission region is also observed in the decay of the ^{268}Sg* nucleus [15], which follows the decay trajectory near $\eta = 0.33$. It is relevant to mention that, usually two fission trajectories are followed by the superheavy composite system, one near the symmetric fission region with $\eta = 0$ (fusion-fission) and the other drags the formed nucleus towards the Pb region with $\eta \sim 0.4$, sometimes associated with the asymmetric quasifission process. The signatures of symmetric quasifission can also be observed around the Sn region [12]. For the decay of the ^{265}Db* nucleus, the potential energy surface (PES), plotted as Fig. 2(c), shows that the fission channel leading to the Pb region diminishes but a new fission channel with mass asymmetry $\eta = 0.29$ opens up, possibly due to the deformation and orientation effects of decaying fragments. The prominent peaks in the mass distribution of ^{265}Db* can be explained further through the contribution of V_C, V_P, and V_ℓ from Fig. 3 plotted at relatively larger radius for the cold orientation approach. The implications of the cold optimum orientation favors interaction of nuclei at further higher values of the radius parameter R (fm), as shown pictorially in Fig. 2(c). For such a configuration, the proximity potential is further enhanced with respect to the dynamic hot-deformed approach, to a significant extent, as depicted in Fig. 3(b). In addition to this, the Coulomb and centrifugal potentials decrease significantly, which drags the fragmentation potential of nuclei to lowest magnitude, leading to the highest preformation yield for asymmetric mass split around the ^{95}Sr and ^{170}Ho fragments. The role of dynamic deformations is also explored for the cold-deformed approach and the preformation yield for the same is shown in the inset of Fig. 2(c). With the inclusion of cold-dynamic deformations, the preformation structure gets modified. Although the peaks around the ^{95}Sr and ^{170}Ho fragments remain intact with a slight modification in magnitude, the symmetric region starts contributing, which is suppressed in the cold-static case. Conclusively, the origin of the symmetric mass split occurs for all the mentioned cases except for the cold-static configurations of the fragments, where the dominance of the fragments around ^{95}Sr and ^{170}Ho nuclei seems evident. Hence from the above discussion, one may conclude that the mass distribution of the fragments is highly dependent on the deformations and orientations of the decay fragments, which is symmetric for the hot fragmentation approach and becomes asymmetric for the cold orientations of the fragments.

B. Evaporation residues and fission cross sections for the ^{267}Db* nucleus

The decay analysis of the ^{238}U-induced reactions is carried out in Sec. III A to address the fusion-fission cross sections

[5] of the ^{265}Db* nucleus. In the recent analysis [6], the experiment was performed for the $Z = 105$ nucleus by using different actinide targets such as ^{248}Cm and ^{249}Bk, and the neutron evaporation residue cross sections were measured. The above-mentioned cross sections are addressed in the framework of the DCM model by using the only parameter of the model, known as neck-length parameter (ΔR). In the fixed neck-length range, the role of the sticking (I_S) and nonsticking ($I_{\rm NS}$) moments of inertia is analyzed in reference to $4n$- and $5n$-decay cross sections of the ^{267}Db* nucleus. In order to understand this, first the comprehensive dynamics of the ^{19}F + ^{248}Cm and ^{18}O + ^{249}Bk reactions is worked out in terms of the capture and fusion of the interacting nuclei and, further, the mass fragmentation of possible decay channels is explored. Elaborating this, primilarly the quantities such as capture cross sections, fusion cross sections, and compound nucleus formation probabilities ($P_{\rm CN}$) are compared for the ^{248}Cm- and ^{249}Bk-induced reactions, followed by the comparison of fission and neutron evaporation of ^{267}Db* nucleus. It is relevant to mention that the fission events for ^{265}Db* nucleus are experimentally measured [5] which are addressed through the DCM framework in the preceding section. However, the fission measurements for ^{267}Db* are not experimentally reported; hence the Wong calculated fusion cross sections are first addressed, so that the $\sigma_{\rm fission}$ be estimated, as $\sigma_{\rm fusion}$ and $\sigma_{\rm fission}$ are related by the relation $\sigma_{\rm fusion} = \sigma_{\rm fission} + \sigma_{\rm EVR}$.

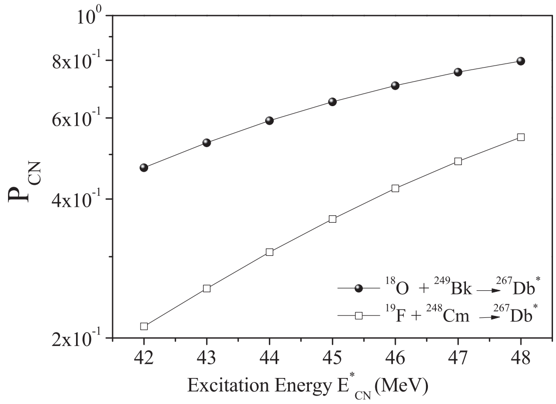

FIG. 5. Compound nucleus formation probability ($P_{\rm CN}$) for ^{267}Db* nucleus formed in the ^{18}O + ^{249}Bk and ^{19}F + ^{248}Cm reactions as a function of excitation energy ($E^*_{\rm CN}$).

Following the above discussion the scattering potential is plotted in Fig. 4 and the barrier characteristics V_B, R_B, and $\hbar\omega$ are extracted. The barrier characteristics have significant influence on the interaction cross sections of the nuclei, as a small change in the Coulomb barrier and distance between colliding nuclei effects the equilibrium between attractive and repulsive forces. Figure 4(a) is plotted to show the barrier characteristics of the ^{267}Db* nuclear system, in which the Coulomb barrier and fusion pockets are depicted for the ^{18}O + ^{249}Bk ($\eta = 0.865$) and ^{19}F + ^{248}Cm ($\eta = 0.857$) reactions. Additionally, the variation of barrier height with energy for the above reactions is plotted in Fig. 4(b) to have a better idea of the barrier characteristics as a function of excitation energy. Lesser barrier height is depicted for the reaction having larger mass asymmetry ($\eta = 0.865$) as the Coulomb factor $Z_1{*}Z_2 = 776$ is relatively lower for the ^{249}Bk-induced reaction compared to $Z_1{*}Z_2 = 864$ for the ^{19}F + ^{248}Cm reaction. This indicates larger fusion probability for the ^{18}O + ^{249}Bk reaction, leading to higher fusion cross sections. Similar results are depicted in Fig. 4(b), indicating a lower barrier height for the ^{18}O + ^{249}Bk reaction over a wide energy range. It is important to mention that the barrier height (V_B) is slightly modified with an increase in energy across the barrier.

Beside barrier characteristics, the compound nucleus formation probability ($P_{\rm CN}$) is an equally important parameter to address the fusion possibility of the interacting nuclei. As evident from Ref. [41], the $P_{\rm CN}$ can be calculated as the ratio of CN fission and capture cross sections. The uncertainties in the measurements of capture cross sections are higher for the superheavy region because the separation of the elastic and quasielastic processes is difficult in the capture events. Also

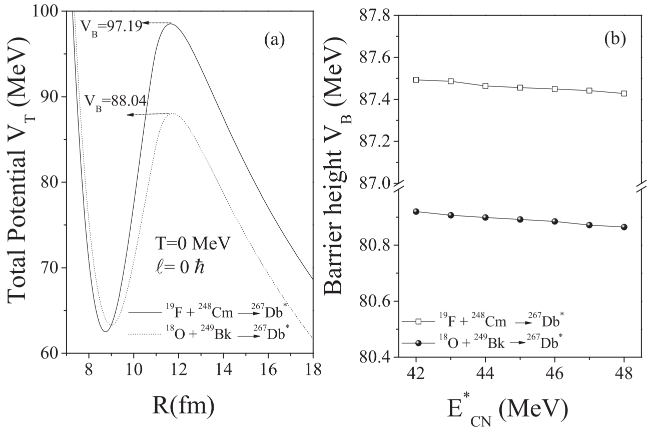

FIG. 4. (a) Total interaction potential (V_T) as a function of range (R) for the ^{267}Db* nuclear system formed via two incoming channels, i.e.,^{19}F + ^{248}Cm and ^{18}O + ^{249}Bk. (b) Barrier heights (V_B) plotted for the above reactions at different excitation energies ($E^*_{\rm CN}$).

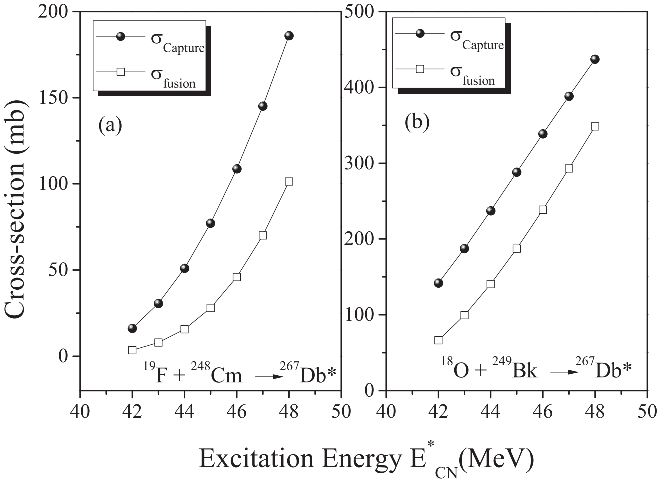

FIG. 6. The Wong predicted capture and fusion cross sections for the reactions (a) ^{19}F + ^{248}Cm and (b) ^{18}O + ^{249}Bk leading to the ^{267}Db* nuclear system at energies near the Coulomb barrier.

TABLE I. DCM fitted fusion-fission cross sections (σ_{ff}) of the ^{265}Db* and ^{267}Db* nuclei formed, respectively, in the ^{27}Al + ^{238}U and (^{19}F + ^{248}Cm, ^{18}O + ^{249}Bk) reactions by using hot compact configurations. The experimentally and theoretically predicted (using Wong model) fusion-fission and capture cross sections are also shown. The contributions of the fusion-fission cross sections to the capture cross sections are also tabulated in percentage form.

E^*_{CN} (MeV)	T (MeV)	ΔR (fm)	σ^{ff}_{DCM} (mb)	ℓ_{max} ($\hbar$)	$\sigma^{ff}_{Exp.}$ (mb)	σ^{ff}_{Wong} (mb)	$\sigma^{Cap}_{Exp.}$ (mb)	σ^{Cap}_{Wong} (mb)	σ_{ff}/σ_{Cap} (%)
^{27}Al + ^{238}U → ^{265}Db*									
49.5	1.45	1.022	83.40	135	85 ± 30	–	160 ± 25	–	53.1%
61.5	1.62	1.040	156.40	140	155 ± 50	–	330 ± 20	–	46.9%
^{19}F + ^{248}Cm → ^{267}Db*									
42.0	1.34	0.978	3.50	114	–	3.43	–	16.17	21.2%
47.0	1.41	1.021	68.20	134	–	70.11	–	145.17	48.3%
^{18}O + ^{249}Bk → ^{267}Db*									
42.0	1.34	1.038	65.80	127	–	66.35	–	141.78	46.8%
47.0	1.41	1.059	292.00	135	–	292.94	–	388.51	75.4%

the contribution of the quasifission process is often unknown. To avoid such uncertainties, the value of P^0_{CN} is estimated by introducing the idea in Ref. [21]. In addition to this, the energy-dependent P_{CN} is calculated using Eq. (11), and the same are plotted in Fig. 5 for the ^{19}F + ^{248}Cm and ^{18}O + ^{249}Bk reactions. The energy range chosen for the calculation of P_{CN} is across the barrier. From this figure it is clearly evident that P_{CN} for ^{267}Db* is larger for relatively asymmetric reaction ^{18}O + ^{249}Bk, and it varies from 0.468 to 0.797. However, for the ^{19}F + ^{248}Cm reaction the magnitude of P_{CN} lies in the range 0.212 to 0.545. This confirms that the fusion probability is much higher for the ^{18}O + ^{249}Bk interacting pair as compared to the ^{19}F + ^{248}Cm reaction. It is also important to note that the compound nucleus formation probability increases with an increase in energy for both reactions, concluding the fact that the nCN processes are more dominant in the sub-barrier region.

Figure 6 shows the calculated capture and fusion cross sections for the ^{267}Db* nucleus formed in the ^{19}F + ^{248}Cm and ^{18}O + ^{249}Bk reactions. The Wong model works nicely near and above the Coulomb barrier, hence the cross sections are calculated for the near barrier energy range $E^*_{CN} = 42-48$ MeV. The figure clearly shows higher capture cross sections than fusion for both reactions, indicating the occurrence of noncompound nuclear processes in the formation of the ^{267}Db* nucleus. The chances of the nCN processes such as quasifission (symmetric or asymmetric) are relatively higher for the ^{19}F + ^{248}Cm reaction due to less fusion probability (see Fig. 5) and lower cross sections [see Fig. 6(a)] for this reaction. On the other hand, the fusion probability for the ^{18}O + ^{249}Bk interacting pair is quite high, leading to higher fusion cross sections. Hence the fusion dynamics is nicely elaborated using the Wong methodology, and the same is subsequently analyzed within DCM by assuming that $\sigma_{fusion} = \sigma_{fission} + \sigma_{EVR}$. The contributions of the fission fragments for the ^{19}F + ^{248}Cm and ^{18}O + ^{249}Bk reactions come mainly through the symmetric mass distribution lying in the range $\frac{A}{2} \pm 15$, the same as observed for the ^{27}Al + ^{238}U reaction [5]. The mass distribution of the fragments for the ^{267}Db* nucleus, formed in the ^{19}F + ^{248}Cm and ^{18}O + ^{249}Bk reactions is not shown here to avoid repetition. On the other hand, the contribution of the evaporation residues is feeble towards the total fusion cross sections, as they are measured in the nb range. Following the above discussion on the fission and evaporation processes, DCM and Wong fitted cross sections are tabulated in Table I for the ^{238}U-, ^{248}Cm-, and ^{249}Bk-induced reactions. The data in Table I are estimated at near-barrier energies, along with the magnitudes of the neck-length parameters.

Finally, the evaporation residue cross sections (nb) of the ^{267}Db* nuclear system, formed in the ^{19}F + ^{248}Cm and ^{18}O + ^{249}Bk reactions are calculated at near-barrier energies,

TABLE II. Comparison of experimental [6] and DCM calculated 4n- and 5n-decay cross sections of the ^{267}Db* nuclear system by including sticking (I_S) and nonsticking (I_{NS}) moment of inertia.

E^*_{CN}	Channel	I_S			I_{NS}			$\sigma_{Expt.}$
(MeV)		ΔR (fm)	σ_{DCM} (nb)	$\ell_{max}(\hbar)$	ΔR (fm)	σ_{DCM} (nb)	$\ell_{max}(\hbar)$	(nb)
42 ± 1	^{19}F + ^{248}Cm (4n)	1.730	0.133	121	1.228	0.127	24	0.127
	^{18}O + ^{249}Bk (4n)	2.471	9.940	102	1.282	9.890	24	10.00
	^{19}F + ^{248}Cm (5n)	2.188	0.222	101	1.288	0.226	25	0.223
	^{18}O + ^{249}Bk (5n)	–	–	–	1.303	1.320	25	1.300
47 ± 1	^{19}F + ^{248}Cm (4n)	1.676	0.064	122	1.200	0.062	24	0.064
	^{18}O + ^{249}Bk (4n)	1.968	2.030	116	1.249	1.920	25	2.030
	^{19}F + ^{248}Cm (5n)	2.419	2.020	116	1.288	1.970	26	2.020
	^{18}O + ^{249}Bk (5n)	–	–	–	1.316	5.770	26	6.010

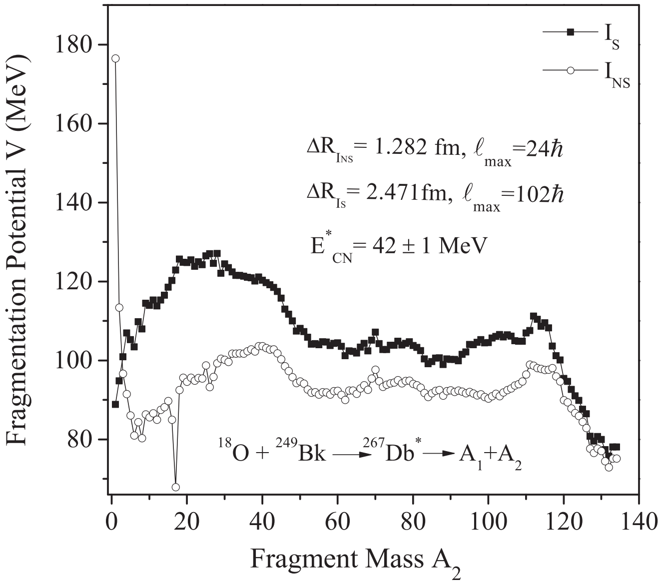

FIG. 7. Fragmentation potential for ^{267}Db* nuclear system plotted as a function of light fragment mass A_2 using sticking (I_S) and nonsticking (I_{NS}) limits of moments of inertia.

using sticking (I_S) and nonsticking (I_{NS}) moments of inertia. Within the I_S approach, $4n$ cross sections are addressed nicely as shown in Table II, but the $5n$ channel of the $^{18}O + {}^{249}Bk$ reaction could not be fitted even at the maximum possible magnitude of the neck-length parameter (ΔR). To address this discrepancy, the fragmentation potential V(MeV) is modified by including the nonsticking (I_{NS}) approach of the moment of inertia, as shown in Fig. 7 and Table II. The fragmentation potentials, plotted in Fig. 7, are presented at the neck-length parameters (ΔR) of the $4n$ clusters of the ^{267}Db* nucleus to obtain the idea about the decay structure. The overview of this figure reveals the fact that structure is significantly modified for the neutron evaporation region, whereas the intermediate mass, heavy mass, and fission regions give a similar fragmentation structure for the I_S as well as the I_{NS} approaches. Broadly speaking, for the use of sticking moment of inertia (I_S), $1n$, $2n$, and $3n$ emissions seem more probable as compare to $4n$ and $5n$ decays. But the exactly opposite trend is observed for the nonsticking (I_{NS}) approach for which the $4n$ and $5n$ channels seems more probable as compared to lighter neutron clusters. Due to the lower fragmentation potential, the $5n$ cross sections are achieved at lower neck-length parameters within the use of the I_{NS} approach. The same is true for the $4n$-decay channel. Within the I_{NS} approach, the neck-length parameters (ΔR) and ℓ_{max} values are reduced significantly. It is to be noted here that, within the I_{NS} limit of moment of inertia, an unexpected minimum is observed for the ^{17}B fragment which is possibly because of the higher deformation ($\beta_2 = -0.398$) of boron. However, when the I_S limit of the moment of inertia is considered, the fragment at $A_2 = 17$ is replaced by ^{17}O ($\beta_2 = 0.107$) and hence no such dip is observed here.

Figure 8 is plotted to compare the fragmentation potential, preformation probability (P_0), and penetrability (P) for the $^{18}O + {}^{249}Bk$ and $^{19}F + {}^{248}Cm$ reactions. The comparison is made to better understand the decay scenario, especially for the $4n$ and $5n$ clusters of the ^{267}Db* nuclear system. It is relevant to mention here that Figs. 8(a)–8(c) are plotted for the $4n$ decay of the ^{267}Db* compound system and the inset shows the same for $5n$ emission at same energy. Figure 8(a) is presented to obtain the variation of fragmentation potential with a wide range of angular-momentum states for both ^{249}Bk- and ^{248}Cm-induced reactions, and it gives a lower magnitude for the $^{18}O + {}^{249}Bk$ reaction, leading to the fact that at same excitation energy, the probability of neutron emission ($4n$ or $5n$) is relatively more prompt for this interacting pair. This result is further supported by Figs. 8(b) and 8(c) which show a larger magnitude of preformation (P_0) and penetration (P) probabilities for the $^{18}O + {}^{249}Bk$ reaction. Also, among $4n$ or $5n$ emission, the probability of $5n$ decay is relatively larger. The magnitude of the neck-length parameters reported in Table II supports the

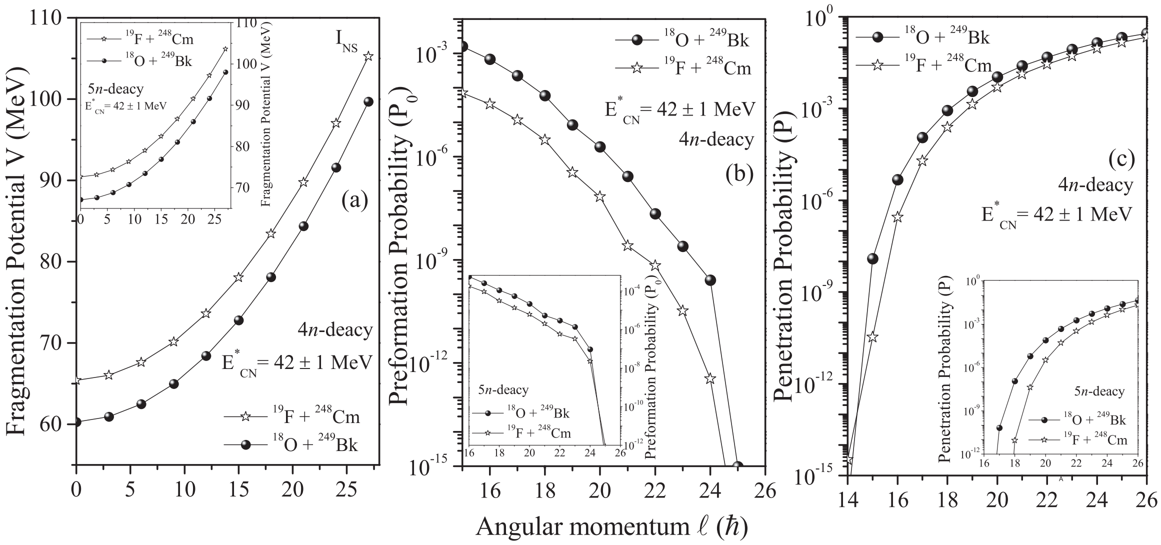

FIG. 8. Variation of the (a) fragmentation potential V(MeV), (b) preformation probability (P_0), and (c) penetration probability (P) for ^{267}Db* nucleus formed in the $^{19}F + {}^{248}Cm$ and $^{18}O + {}^{249}Bk$ reactions, plotted as a function of angular momentum for $4n$ and $5n$ decays.

above result as higher magnitude of the neck-length parameters are reported for the 5n emission within the $I_{\rm NS}$ approach. A larger neck leads to easier splitting of the cluster from the excited nucleus. Hence one may conclude that the probability of neutron emission is higher for the nucleus formed in the ^{18}O + ^{249}Bk reaction and out of 4n and 5n emission, 5n decay is relatively more prompt.

IV. SUMMARY

In the present work, the fragmentation potential and preformation yields are calculated for the ^{265}Db* nucleus. Symmetric mass distribution of the fission fragments is observed for the static-hot optimum orientation approach, leading to the fact that fusion-fission is the dominant decay mode for the ^{265}Db* compound nucleus. Further the PES of the ^{265}Db* nuclear system is compared with neighboring nuclei such as ^{264}Rf* and ^{268}Sg*, resulting in similar symmetric fragmentation behavior. The peaks around the Pb region in the preformation yield do not significantly contribute towards the total cross sections, and hence the chances of the quasifission channels are small when the hot orientation approach is used. The dynamical hot orientations are also applied to study the preformation yield of ^{265}Db* nucleus, and relatively broad fission distribution is observed with fragments lying in the range $\frac{A}{2} \pm 25$. The small preformation probability of the peaks around $A_2 = 95$ in the hot-static case gets significantly enhanced for the dynamical approach, which could be explained on the basis of the interplay between various attractive/repulsive forces contributing towards fragmentation potential. Finally, asymmetric preformation distribution is obtained for the static-cold approach at mass asymmetry $\eta = 0.29$, resulting in a new fission region which is different from the traditional superheavy decay of fusion-fission ($\eta \sim 0$) and quasifission ($\eta \sim 0.4$). The dynamical deformations are also tested within the cold orientation approach, which gives a modified preformation structure, where the contribution of symmetric fragments again dominates.

The fission and evaporation decay channels are also investigated for ^{267}Db* nuclear system formed in the ^{19}F + ^{248}Cm and ^{18}O + ^{249}Bk reactions. To compare the entrance channel relevance, the barrier characteristics are calculated for both reactions, resulting in smaller barrier height for the ^{18}O + ^{249}Bk reaction. The capture and fusion cross sections are calculated using the Wong model. Higher fusion cross sections are obtained for the ^{18}O + ^{249}Bk channel as compared to ^{19}F + ^{248}Cm, due to smaller Coulomb repulsion in the entrance channel. The compound nucleus formation probability ($P_{\rm CN}$) for the ^{18}O + ^{249}Bk reaction is relatively larger as compared to ^{19}F + ^{248}Cm. Finally, the 4n and 5n evaporation residue cross sections are calculated for the ^{19}F + ^{248}Cm and ^{18}O + ^{249}Bk reactions using sticking (I_S) and nonsticking ($I_{\rm NS}$) approaches of the moments of inertia. The 4n cross sections for both reactions are addressed nicely within the I_S and $I_{\rm NS}$ approaches, whereas only the nonsticking moment of inertia could address the 5n cross sections of the ^{18}O + ^{249}Bk reaction. Further, the fragmentation analysis of the 4n and 5n decays support prompt emission of 5n clusters.

ACKNOWLEDGMENT

The financial support from the Depeartment of Science and Technology (DST), in the form of Grant No. EMR/2016/000008, is gratefully acknowledged. G.K. is thankful to DST, New Delhi, for the INSPIRE fellowship (Grant No. DST/INSPIRE/03/2015/000199).

---

[1] Y. T. Oganessian *et al.*, Phys. Rev. C **76**, 011601(R) (2007); Phys. Rev. Lett. **108**, 022502 (2012); Phys. Rev. C **87**, 014302 (2013); **83**, 054315 (2011).
[2] R. C. Barber *et al.*, Pure Appl. Chem. **65**, 1757 (1993).
[3] J. M. Gates *et al.*, Phys. Rev. C **78**, 034604 (2008).
[4] H. G. Clerc *et al.*, Nucl. Phys. A **419**, 571 (1984).
[5] W. Q. Shen *et al.*, Phys. Rev. C **36**, 115 (1987).
[6] H. Haba *et al.*, Phys. Rev. C **89**, 024618 (2014).
[7] R. K. Gupta, Niyti, M. Manhas, and W. Greiner, J. Phys. G: Nucl. Part. Phys. **36**, 115105 (2009); K. Sandhu, M. K. Sharma, A. Kaur, and R. K. Gupta, Phys. Rev. C **90**, 034610 (2014).
[8] Niyti, R. K. Gupta, and W. Greiner, J. Phys. G: Nucl. Part. Phys. **37**, 115103 (2010).
[9] K. Sandhu, M. K. Sharma, and R. K. Gupta, Phys. Rev. C **85**, 024604 (2012); R. Kumar, K. Sandhu, M. K. Sharma, and R. K. Gupta, *ibid.* **87**, 054610 (2013).
[10] K. Sandhu, M. K. Sharma, and R. K. Gupta, Phys. Rev. C **86**, 064611 (2012).
[11] K. Sandhu, G. Kaur, and M. K. Sharma, Nucl. Phys. A **921**, 114 (2014).
[12] G. Kaur, K. Sandhu, and M. K. Sharma, Phys. Rev. C **94**, 014615 (2016).
[13] M. G. Itkis *et al.*, Nucl. Phys. A **787**, 150c (2007); M. G. Itkis, I. M. Itkis, G. N. Knyazheva, and E. M. Kozulin, *ibid.* **834**, 374c (2010).
[14] C. Y. Wong *et al.*, Phys. Rev. Lett. **31**, 766 (1973).
[15] K. Nishio *et al.*, Phys. Rev. C **82**, 024611 (2010); **82**, 044604 (2010).
[16] D. L. Hill and J. A. Wheeler, Phys. Rev. **89**, 1102 (1953); T. D. Thomas, *ibid.* **116**, 703 (1959).
[17] S. C. Miller, Jr. and R. H. Good, Jr., Phys. Rev. **91**, 174 (1953).
[18] D. Jain *et al.*, Eur. Phys. J. A **50**, 155 (2014).
[19] E. M. Kozulin *et al.*, Phys. Rev. C **94**, 054613 (2016).
[20] R. du. Rietz *et al.*, Phys. Rev. C **88**, 054618 (2013).
[21] V. I. Zagrebaev and W. Greiner, Nucl. Phys. A **944**, 257 (2015); Phys. Rev. C **78**, 034610 (2008).
[22] J. Maruhn and W. Greiner, Phys. Rev. Lett. **32**, 548 (1974).
[23] R. K. Gupta, W. Schied, and W. Greiner, Phys. Rev. Lett. **35**, 353 (1975).
[24] P. Holzer, U. Mosel, and W. Greiner, Nucl. Phys. A **138**, 241 (1969); J. Maruhn and W. Greiner, Z. Phys. **251**, 431 (1972).
[25] R. A. Gherghescu, Phys. Rev. C **67**, 014309 (2003).
[26] H. Kröger and W. Scheid, J. Phys. G: Nucl. Phys. **6**, L85 (1980).
[27] D. R. Inglis, Phys. Rev. **96**, 1059 (1954); S. T. Belyaev, Mat. Fys. Medd. Dan. Vid. Selsk **31**(11) (1959).

[28] S. Kumar, R. K. Gupta, and W. Scheid, Int. J. Mod. Phys. E **3**, 195 (1994); R. K. Gupta and W. Greiner, *ibid.* **3**, 335 (1994).

[29] S. S. Malik and R. K. Gupta, J. Phys. G: Nucl. Phys. **12**, L161 (1986).

[30] N. J. Davidson *et al.*, Nucl. Phys. A **570**, 61c (1994).

[31] P. A. Seeger, Nucl. Phys. **25**, 1 (1961).

[32] W. Myers and W. J. Swiatecki, Nucl. Phys. **81**, 1 (1966).

[33] V. M. Strutinsky, Nucl. Phys. A **95**, 420 (1967); **122**, 1 (1968).

[34] G. Audi, A. H. Wapstra, and C. Thibault, Nucl. Phys. A **729**, 337 (2003).

[35] P. Möller, J. R. Nix, W. D. Myers, and W. J. Swiatecki, At. Data Nucl. Data Tables **59**, 185 (1995).

[36] K. Alder and A. Winther, Nucl. Phys. A **132**, 1-4 (1969).

[37] R. K. Gupta *et al.*, J. Phys. G: Nucl. Part. Phys. **31**, 631 (2005).

[38] A. Jensen and J. Damgaard, Nucl. Phys. A **203**, 578 (1973); M. Muenchow and W. Scheid, Phys. Lett. B **162**, 265 (1985); M. Rashdan, A. Faessler, and W. Waida, J. Phys. G: Nucl. Part. Phys. **17**, 1401 (1991).

[39] R. K. Gupta, N. Singh, and M. Manhas, Phys. Rev. C **70**, 034608 (2004).

[40] G. Royer and J. Mignen, J. Phys. G: Nucl. Part. Phys. **18**, 1781 (1992).

[41] S. Chopra, A. Kaur, and R. K. Gupta, Phys. Rev. C **91**, 034613 (2015).